INTERACTION OF PLASMA
WITH SURFACES

Sputtering Yields of Beryllium and Tungsten by Various Atoms from Hydrogen to Tungsten

V. S. Mikhailov[a], P. Yu. Babenko[a],*, A. P. Shergin[a], and A. N. Zinoviev[a]

[a]Ioffe Institute, Russian Academy of Sciences, St. Petersburg, 194021 Russia

*e-mail: babenko@npd.ioffe.ru

Abstract—Sputtering yields of targets made of Be and W, promising materials for the first wall and the divertor of the ITER tokamak, are calculated in a wide range of projectile energies from 10 to 100 000 eV by computer simulation. The following atoms were chosen as bombarding particles: H, D, T, He, Be, C, N, O, Ne, Ar, and W. It is demonstrated that the shape of the surface strongly impacts the obtained results. The limiting cases of a planar potential barrier (a smooth surface) and a spherical potential barrier (a rough surface) are analyzed. The data on the average energy and angular distribution of sputtered atoms needed for calculation of the impurity influx into tokamak plasma are obtained. The influx of atoms of the wall material into the ITER tokamak plasma upon wall sputtering by fluxes of fast deuterium and tritium atoms leaving plasma is estimated.

1. INTRODUCTION

International project aimed at creation of an ITER tokamak-reactor is an important step on the way to achieving a controlled fusion. Materials of the first wall and the divertor (beryllium and tungsten) will be subjected to the action of high-intensity fluxes of fast atoms, ions, electrons, neutrons, and radiation. An influx of any significant amount of impurities into plasma can terminate the fusion reaction.

We calculated the sputtering yields of beryllium and tungsten by hydrogen isotopes earlier [1−3]. We also obtained energy distributions of the sputtered particles. The obtained data are important for calculation of the influx of sputtered particles into the hot zone of plasma.

It is known that fusion reaction is accompanied by production of helium. Carbon, nitrogen, and oxygen represent impurities in plasma. As a rule, they are produced as a result of chemical reaction from carbides, nitrides, and oxides upon bombardment of construction materials by hydrogen isotopes. Nitrogen, neon, and argon can be added into plasma to reduce the plasma temperature in the near-wall area.

To reduce radiative energy losses by plasma upon influx of the wall material into plasma, the wall is planned to be fabricated from beryllium, a material with low atomic number Z. It was demonstrated in [4] that wall stuttering by deuterium and tritium atoms can cause an influx of beryllium into the separatrix region. In the process, concentration of beryllium can reach 2−4% of the plasma density.

The electron temperature in the separatrix region can be as high as 100−150 eV, and the electron density can reach 10^{13} particles/cm^3 [5]. Under these conditions, the impurity particles are present in plasma in the form of multiply charged ions. Upon bombardment of the divertor, the impurity ions are accelerated by the plasma−wall potential, and their energy increases substantially. The impurity ions can thus cause much larger sputtering of the divertor than the hydrogen atoms. Therefore, reliable information on the sputtering yields of beryllium and tungsten by impurities is important for estimating the functionality of the materials used in the ITER tokamak.

The widely used SRIM code [6] yields incorrect results when used for calcualtion of sputtering dominated by the flux of the back-scattered particles. This is because the code calculates scattering by using the magic expressions that yield incorrect results in the case of large-angle scattering. There is an SPTrimSP (SP means Sputtering) modification of the code that is free of this drawback. Detailed calculations of the sputtering yields by means of the SPTrimSP code for various materials were carried out in [7, 8] within the framework of the pair-interaction approximation using the KrC interatomic interaction potential. The present work aims at conducting more accurate calculation of the sputtering yields by using an up-to-date information on the multi-particle potentials [9−13] and correction of the concepts of electronic stopping powers taking into account collision multiplicity that we proposed in [14].
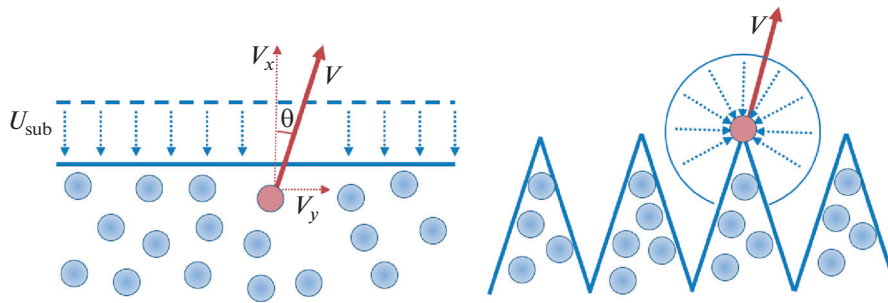
Fig. 1. The shape of the potential barrier for different surfaces: (a) planar barrier (smooth surface), (b) spherical barrier (the surface consisting of points). Solid arrow shows the propagation direction of the sputtered particle. Dotted arrows show the direction of the electric-field lines.

2. THE METHOD

Simulations were carried out using the code that we developed based on the Monte Carlo method. The simulation started with calculation of the projectile trajectory and terminated when the particle was ejected into vacuum (back scattering) or when the particle energy dropped below a certain value (2 eV) in the course of its stopping in the material. We usually calculated one million projectile trajectories with random initial conditions to accumulate the necessary statistics. The number of incident particles was increased to 100 million when calculating the sputtering yield close to the threshold. Pair potentials obtained within the framework of the density functional theory that were in agreement with the experimental data obtained in the studies of gas-phase scattering [15] were used for calculation of the trajectories. Corrections taking into account the potential-well parameters were introduced according to [16].

Reliable experimental data for aluminum [17] scaled taking into account the difference in electron density of beryllium, tungsten, and aluminum by means of the method proposed in [18], along with correction for collision multiplicity [14], were used for description of the electron stopping losses.

The target was described as a set of microcrystals of the material under consideration with a size of one lattice period that were randomly oriented in space. The target surface was defined as an arbitrary cut of the crystal. Thermal vibrations of the target atoms were taken into account. In the process, the vibrational amplitude was specified at room temperature.

An incident particle creates fast recoil particles upon collisions with the target atoms. The set of coordinates, energies, and vectors of velocity of these particles was recorded in a data file. The recoil particles can, in turn, generate a cascade of particles the corresponding parameters of which were also entered into the data file. The recoil-particle trajectories were calculated using multi-particle potentials obtained using the density functional theory [9–13]. Particles penetrating the surface potential barrier and emerging into vacuum were assumed sputtered.

The model of the potential barrier at the solid–vacuum interface [19] substantially influences the simulation results. The model depends on the surface topography (Fig. 1). The surface potential can be assumed isotropic (spherical) for the surface consisting of atomic-scale points. In this case, energy E_2 of the sputtered particle must be higher than the sublimation energy E_s. The model of a planar potential was used for the smooth surface. In the latter case, condition $E_2\cos^2(\Theta) > E_s$, where Θ is the angle at which the sputtered particle emerges from the target relative to the surface normal, must be fulfilled for the sputtered particle.

The dependence of the sputtering yield on the angle of incidence of the beam on the target and the effect of redeposition must be taken into account when calculating sputtering of the surface exhibiting macroscopic roughness. Under real tokamak operating conditions, the surface roughness can vary considerably. Therefore, we calculated the sputtering yields only for the two limiting cases discussed above.

3. SPUTTERING YIELDS OF BERYLLIUM AND TUNGSTEN BY H, D, T, He, C, N, O, Ne, Ar, AND W ATOMS

Sputtering yields of beryllium by H, D, T, He, C, N, O, Ne, and Ar atoms are presented in Fig. 2 as a function of projectile energy for two limiting cases of the surface potential barrier.
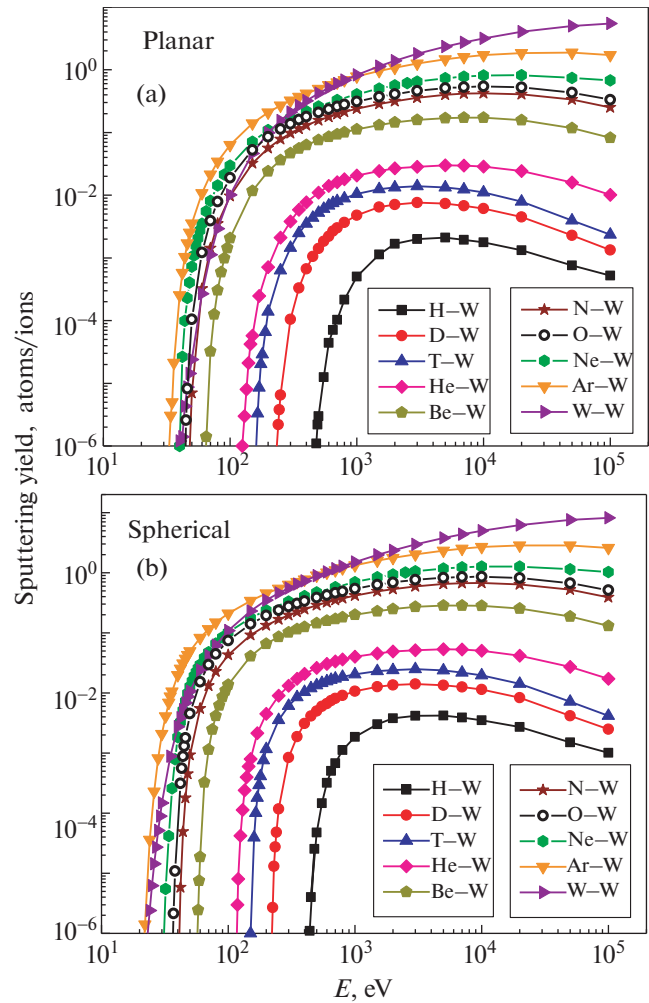
It is evident from Fig. 2 that calculations produse higher values of the sputtering yield for the spherical barrier, which is related to selection condition of the sputtered particles. The dependences of the sputtering yield on collision energy are drastically different for the cases of $M_1 > M_2$ and $M_1 < M_2$. Here, M_1 and M_2 are the masses of the projectile and the target atom, respectively. Position of the energy threshold for the dependence of the sputtering yield on the projectile energy changes upon change in the projectile mass.
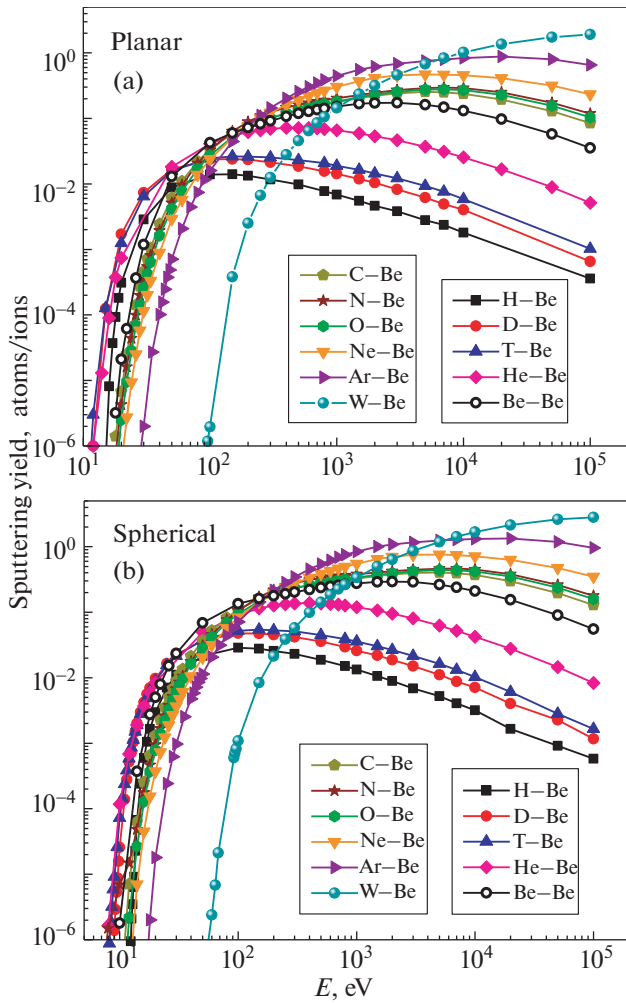
Fig. 2. Sputtering yields of a beryllium target by H, D, T, He, C, N, O, Ne, and Ar atoms for normal beam incidence as a function of projectile energy: (a) planar barrier, flat surface; (b) spherical barrier, the surface consisting of individual atoms.

Fig. 3. Sputtering yields of a tungsten target by H, D, T, He, C, N, O, Ne, Ar, and W atoms for normal beam incidence as a function of projectile energy: (a) planar barrier, flat surface; (b) spherical barrier, the surface consisting of individual atoms.

The physical model of sputtering is different for the cases mentioned above. When a light particle collides with a heavy atom ($M_1 < M_2$), sputtering of the near-surface layers by the back-scattered light atoms is dominant. This case was analyzed in [20]. Single scattering of a projectile at an angle larger than arcsin(M_1/M_2) is impossible when $M_1 > M_2$, and sputtering occurs due to the development of a cascade of collisions of target particles. This case is described by the Sigmund theory [21].

Sputtering yields calculated for the tungsten target are presented in Fig. 3. The projectile mass was lower than that of the target atom in all cases except the W−W collision. The sputtering yield grows with increase in the projectile mass. Similar to the case of beryllium, sputtering yields are larger for the spherical potential barrier than for the planar one.

Comparison of Figs. 2 and 3 shows that the relation between the masses of the interacting particles is an important factor that influences the behavior of the sputtering-yield dependence on the projectile energy under normal incidence.

4. ANALYSIS OF THE SPUTTERING THRESHOLDS

We assume that the collision energy at which the sputtering yield tends to zero represents the sputtering threshold. Let us analyze the case of sputtering of a heavy target by a light particle first. Energy Q imparted to the surface atom must exceed the surface binding energy E_s, i.e., $Q = \gamma E_1 > E_s$. Here, $\gamma = 4M_1M_2/(M_1 + M_2)^2$, M_1 and M_2 are the masses of the projectile and
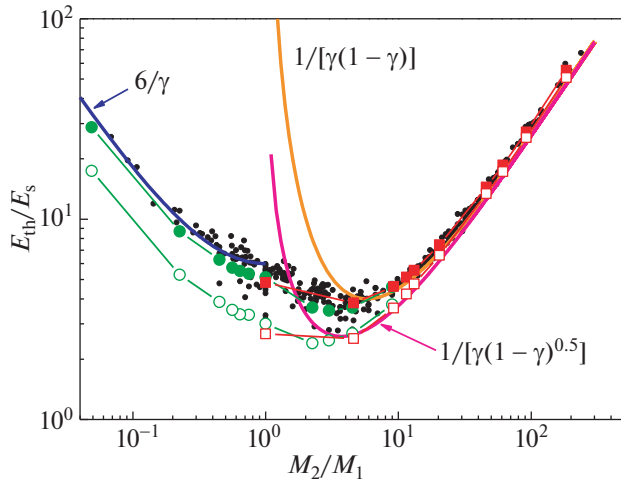
Fig. 4. The ratio of the threshold sputtering energy to the sublimation energy as a function of mass of colliding particles. The calculation results are given for Be target ((circles) pherical barrier and (filled circles) planar barrier) and W target ((squares) spherical barrier and (filled squares) planar barrier). Small black dots illustrate the results obtained in [6]. The curves represent the results of approximation (see text for details).

the target atom, respectively, while E_1 is the maximum energy of the back-scattered particles.

In order to knock out a surface atoms, the projectile must turn by $90°-180°$. The particle energy after single scattering at angle θ in the laboratory frame of reference is described by the following equation:

$$\frac{E_1}{E_0} = \left(\frac{M_1}{M_1 + M_2}\right)^2 \left[\cos\theta \pm \left[\left(\frac{M_2}{M_1}\right)^2 - \sin^2\theta\right]^{0.5}\right]^2. \quad (1)$$

When the projectile turns by $90°$, its energy is given by $E_1 = (M_2 - M_1)/(M_1 + M_2)E_0$, where E_0 is the initial energy. When the particle turns by $180°$, it energy is equal to $E_1 = (M_2-M_1)^2/(M_1 + M_2)^2 E_0$. Combining the conditions of energy transfer to the recoil particle and the energy loss caused by change in the particle trajectory, we find that $Q = \gamma E_1 = \gamma(1 - \gamma)^{0.5}E_0$ for an angle of $90°$ and $Q = \gamma E_1 = \gamma(1 - \gamma)E_0$ for an angle of $180°$. The threshold energy is thus given by $E_{th} > E_s/[\gamma(1 - \gamma)^{0.5}]$ for the angle of $90°$ and $E_{th} > E_s/[\gamma(1-\gamma)]$ for the angle of $180°$. The latter equation was derived earlier in [22].

It is evident from Fig. 4 that the condition for the turn angle of $180°$ describes the data for $M_2/M_1 > 4$ for planar barrier quite well, while our condition describes the data for the spherical barrier better. It should be noted that multiple collisions lead to higher energy E_1 than the single ones. It was demonstrated in [2] that this correction substantially changes the threshold for the cases of H, D, and T−Be.

Let us analyze the case of $M_2 > M_1$. The mechanism of sputtering by a flux of back-scattered ions does not work in this case. The energy imparted to the recoil particle upon the first collision is given by $Q = \gamma E_0$. After that, the particle continues moving into the solid. At least several collisions of particles of equal mass are required in order for the projectile trajectory to turn by $90°-180°$. It can be seen from Fig. 4 that the empirical dependence given by $E_{th}/E_s = 6/\gamma$ describes the data for the case of $M_2/M_1 < 1$ reasonably well.

5. COMPARISON OF SPUTTERING YIELDS OF BERYLLIUM AND TUNGSTEN WITH THE DATA REPORTED BY OTHER AUTHORS

Let us compare the obtained results with the data of other authors for a number of cases. The dependences of sputtering yield of beryllium on the energy of the bombarding beam of He, Be, O, Ne, and Ar atoms are presented in Fig. 5. Depicted are the results of our calculations for the planar and spherical potential barriers at the solid−vacuum interface. It can be seen that the experimental data and the results of calculations carried out by the Eckstein group [7] fall between the two limiting cases analyzed in the present work.

There is a large scatter of the experimental data in the case of He−Be. Unfortunately, no experimental data is available for all cases near the threshold. Experimental data for the cases of Be−Be and Ar−Be lie closer to the results of our calculations for the spherical barrier.

The authors of [20] proposed an equation governing sputtering yield Y of heavy targets upon their bombardment by low-energy particles that has the form

$$Y = 1.276 E_s^{-1} \frac{Z_1 Z_2}{(Z_1^{2/3} + Z_2^{2/3})^{1/2}} \frac{\mu - 1}{(1 + \mu)^2} F(w), \quad (2)$$

where Z_1 and Z_2 are the charges of the colliding atoms, $\mu = M_2/M_1$, and

$$F(w) = \frac{\ln w + 3w^{-1/2} - \left(3w^{\frac{3}{2}}\right)^{-1} - 8/3}{w^{1/2}}, \quad (3)$$

$$w = \frac{E_0}{E_{th}}, \quad E_{th} = \frac{E_s}{\gamma(1 - \gamma)}.$$

Here, E_{th} is the threshold sputtering energy, and E_0 is the energy of an incident atom.

Equation (2) is applicable only in the case of $M_1 < M_2$ and works particularly well when $M_1 \ll M_2$. It can be seen from Fig. 5 that the expression does not work well in the case of He−Be.

The dependences of the sputtering yield of a tungsten target on the energy of bombarding atoms of He, Be, O, Ne, Ar, and W are presented in Fig. 6. The results of calculation based on Eq. (2) for the Ne−W
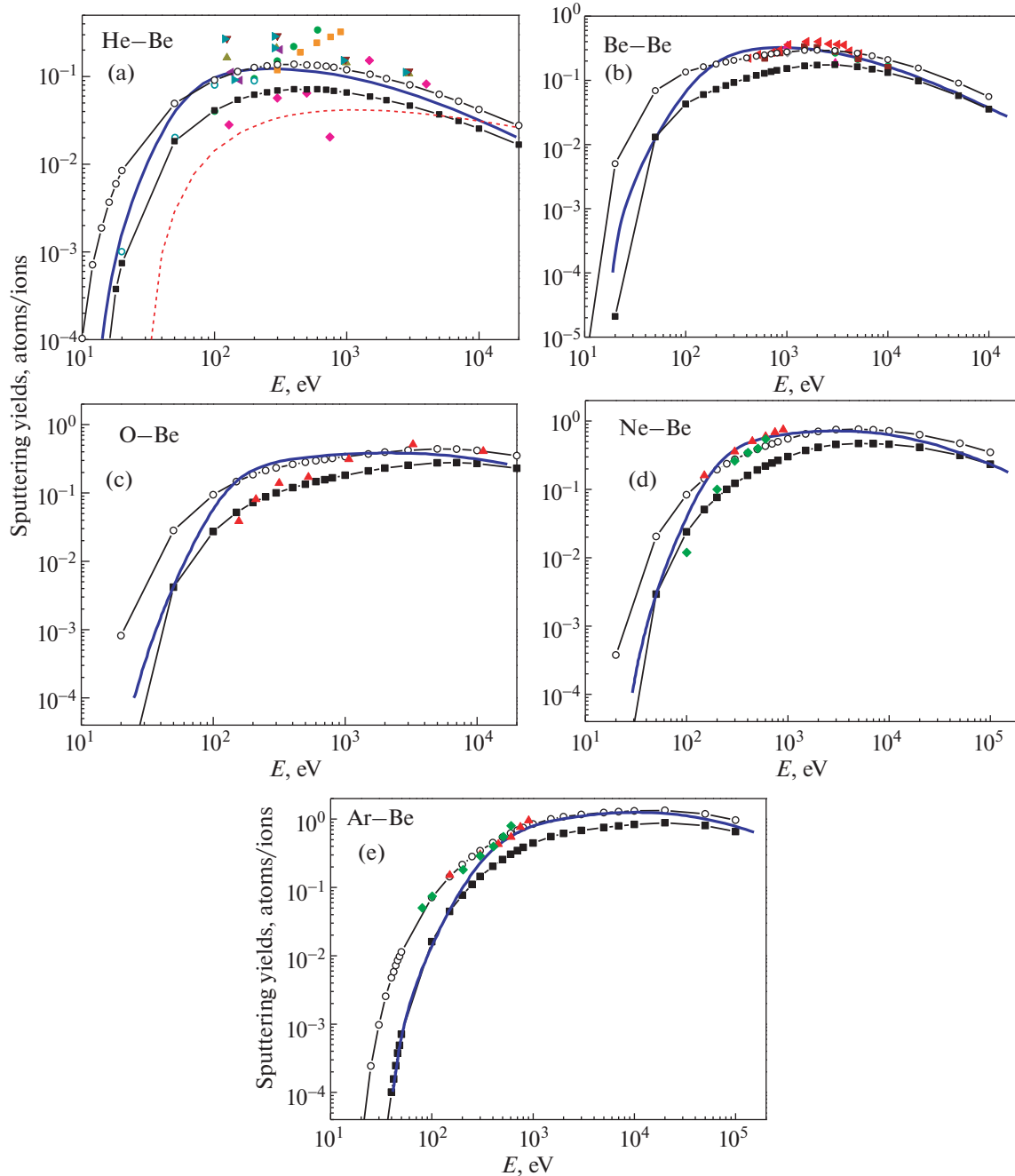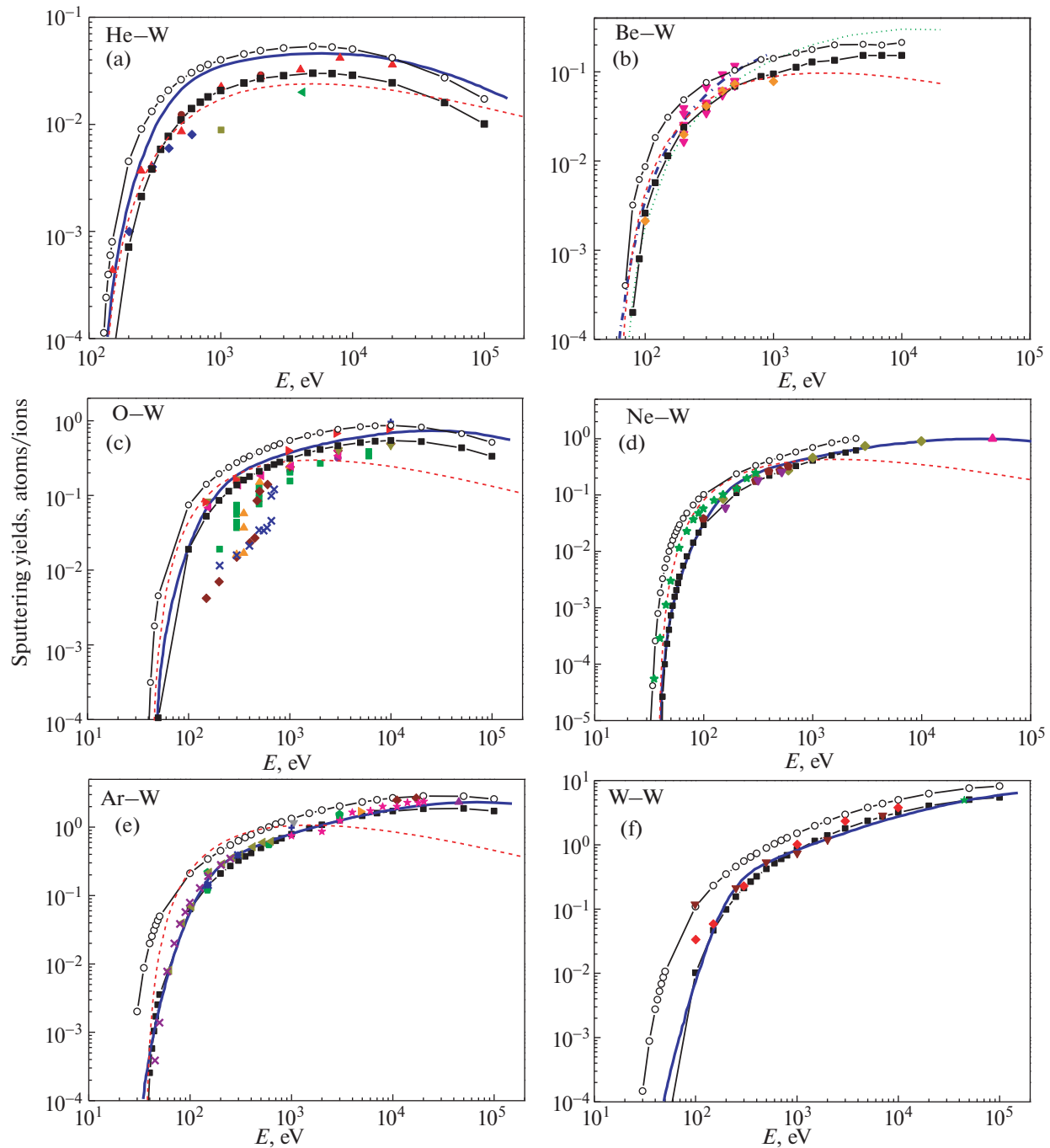
Fig. 5. Sputtering yields of beryllium target by atoms of He (a), Be (b), O (c), Ne (d), and Ar (e) as a function of energy of bombarding particles. The calculation results are given for (curve with squares) planar barrier and (curve with circles) spherical barrier; (solid blue curve) result of calculation by the Eckstein group [7]; (dots) experimental results adopted from [6]. Dashed curve in Fig. 5a represents the result of calculation using Eq. (2) [19].

and Ar–W pairs are illustrated by the dashed line. The discussed expression underestimates the sputtering yield at energies below 1000 eV. The results of calculations carried out by the Eckstein group [7, 8] lie close to our results for the case of a planar target surface. The experimental data for the cases under consideration also group close to the results of calculations for

the case of a planar barrier. This could be related to high surface quality of the studied target.

The results of calculations conducted by the Eckstein group for the cases of He–W and O–W fall between the results of our calculation for the two surface potential barriers, and the results of our calculations for the planar potential agree well with the results

Fig. 6. Sputtering yields of a turngsten target by atoms of He (a), Be (b), O (c), Ne (d), Ar (e) and W (f) as a function of energy of bombarding particles. The calculation results are given for (curve with squares) planar barrier and (curve with circles) spherical barrier; (solid blue curve) result of calculation by the Eckstein group [6, 7]; (dots) experimental results adopted from [6]. The dashed line represents the result of calculation using Eq. (2) [19]. For the Be−W case, the results of calculations (squares and tri-angles) using the molecular dynamics approach [22, 23], (dotted curve) using expressions derived in [24], and (dash-dotted curve) by means of the SDTrimSP code [25] are also presented.

obtained by the Eckstein group and the experimental data in the cases of Ne−W, Ar−W, and W−W. The experimental data exhibit large scatter in the case of He−W. No experimental data is available for the Be−W case, but our results agree well with the results of

calculations carried out by the methods of molecular dynamic [23, 24] along with the calculations based on the expression obtained in [25] and the SDTrimSP code [26]. The calculation based on the Falcone the-ory is not applicable in the W−W case. This approach

describes well the energy dependence of the sputtering yield from the threshold to the energy of $E_0 \approx 3$ keV in other cases but considerably underestimates the sputtering yield at high energies.

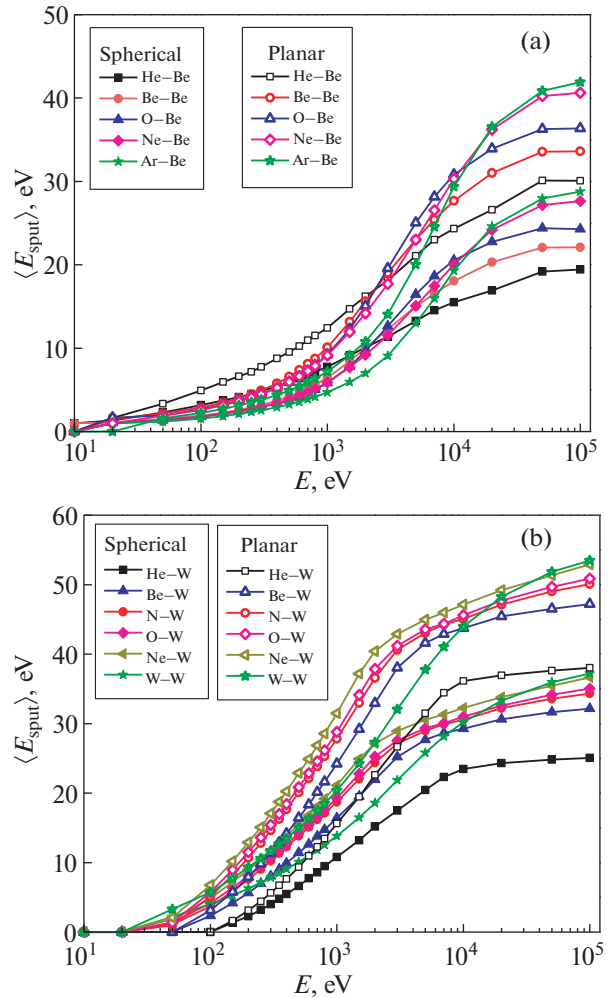## 6. THE AVERAGE ENERGY OF THE SPUTTERED PARTICLES

It can be seen from Fig. 7 that the average energy of the sputtered particle grows with increase in the projectile energy. The growth slows down at collision energy exceeding 10 keV. The average energy of the sputtered particle grows also with increase in the projectile mass. For the planar surface barrier, the average energy of the sputtered particle is higher since the sputtered particles with low energy do not satisfy the selection condition that has the form $E_2\cos^2(\Theta) > E_s$. At collision energies higher than 1 keV, the ratio of the average energies of particles for the planar and spherical barriers remains nearly constant and falls in the range of 1.53−1.61 for the beryllium target and 1.45−1.49 for the tungsten one. This means that the average value of $\cos^2(\Theta)$ averaged taking into account the angular distribution of the sputtered particles is equal to 0.66−0.71. The estimated angle at which a sputtered particle emerges from the target is thus equal to $\Theta \approx 33°−36°$.

Information on the average energies of sputtered atoms is needed to obtain an estimate of the probability of penetration of sputtered particles through the near-wall plasma layer.

7. THE ANGULAR DISTRIBUTIONS OF THE SPUTTERED PARTICLES

The angular distribution of the sputtered particles normalized to its peak value has a universal character for all studied cases in a wide range of collision energies ($E_0 > 1$ keV). It can be seen from Fig. 8 that the angular dependence attains maximum at $\Theta \approx 35°$. Small differences are observed only at collision energies close to the sputtering threshold. Comparison of cases *a* and *b* demonstrates universality of also the angular dependence as a function of mass of the target atom, while comparison of cases *b* and *c* demonstrates its universality as a function of the projectile mass. The angular distribution in the case of spherical surface barrier reflects the angular distribution of the sputtered particles before they leave the solid.

It can be seen from Fig. 8c that, at low collision energies, i.e., near the sputtering threshold, some particles emerge at an angle of 60°−75° relative to the surface normal. A multiple (double or triple) scattering takes place in this case, and the total deviation angle of the particle trajectory is about 105°−120°. Single scattering does not contribute to sputtering in the case of $M_2 \geq M_1$.

Fig. 7. Average energy of a sputtered atom as a function of initial energy of the bombarding particle for various incident atoms: (a) Be target, (b) W target. Filled symbols correspond to a planar surface barrier, while unfilled symbols correspond to a spherical barrier.

The normalized angular distributions for the planar surface barrier are presented in Fig. 9.
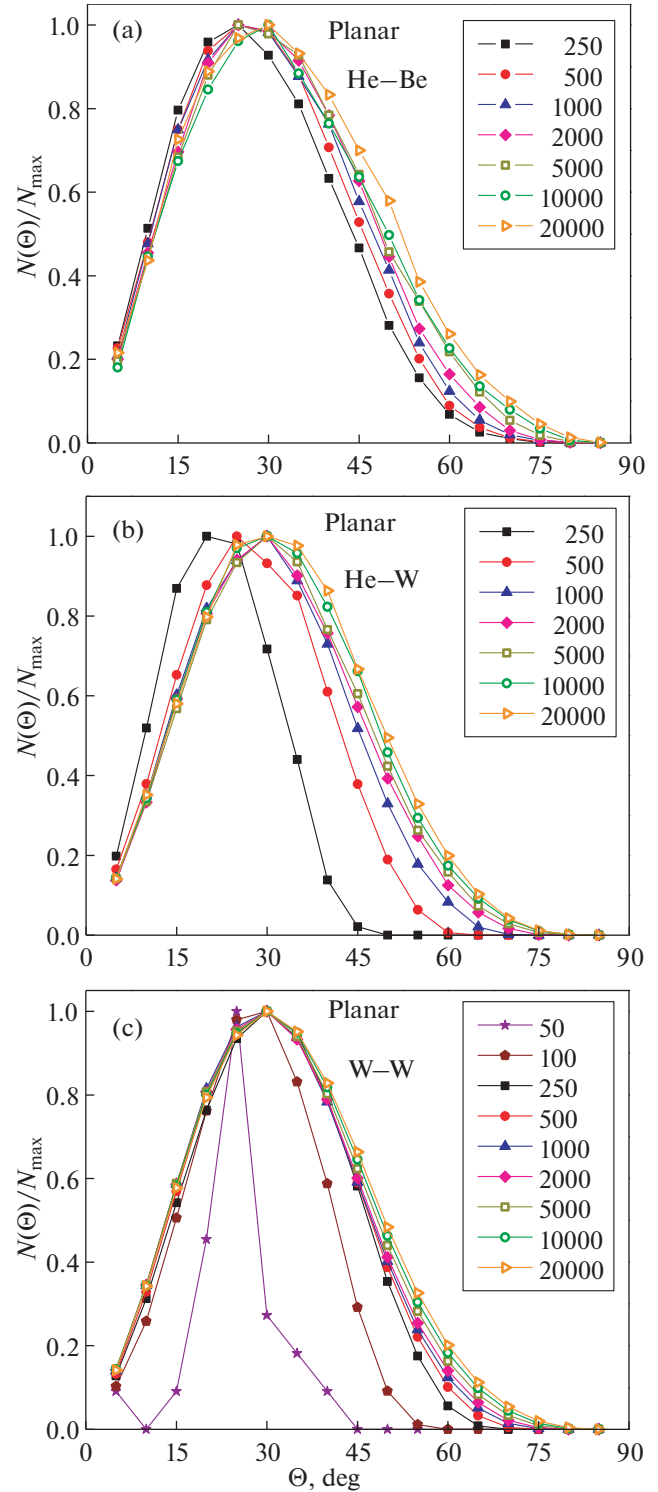
The normalized angular distribution in the case of a planar surface barrier does not have a universal character, which is related to the sputtered-particle selection condition $E_2\cos^2(\Theta) > E_s$. The angular distribution approaches the shape typical of the spherical potential barrier with increase in the projectile energy.

Single scattering does not contribute to sputtering in the case of W−W collisions. There are particles emerging at an angle of 20° relative to the surface normal due to the selection criterion of the sputtered particles for the planar potential near the threshold. This means that a larger total deviation angle of about 160° is accumulated due to multiple scattering, which results in a large energy loss by the sputtered particles. The observed difference in the total deviation angle of
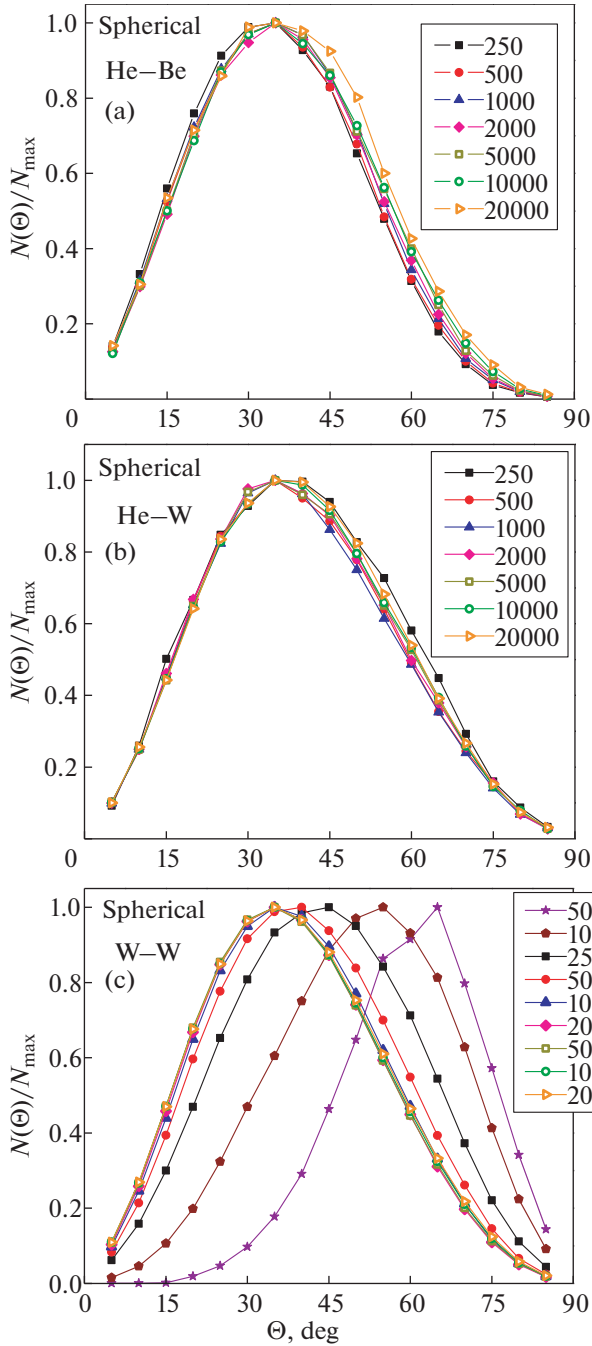
Fig. 8. Normalized angular distribution of sputtered particles for the case of a spherical surface potential barrier: (a) He−Be; (b) He−W; (c) W−W.

Fig. 9. Normalized angular diatributions of sputtered particles for the case of a planar surface potential barrier: (a) He−Be; (b) He−W; (c) W−W.

the particle trajectory upon multiple collisions for the spherical and planar potential barriers changes the ratio E_{th}/E_s for these cases (Fig. 4). To clarify this statement, let us analyze an example, namely, the case of triple scattering of particles of equal mass. Particle energy after each collision upon scattering at angle Θ is given by $E_2 = E_0\cos^2\Theta$. After three collisions and scattering at angle Θ, the particle energy is thus given

by $E_4 = E_0\cos^6\Theta$. The total deviation angle of $\Theta_\Sigma = 120°$ is sufficient for the spherical barrier at collision energy close to the threshold, and thus $E_4 = E_0\cos^6(\Theta_\Sigma/3) = E_0 \times 0.202$. For the planar barrier, we
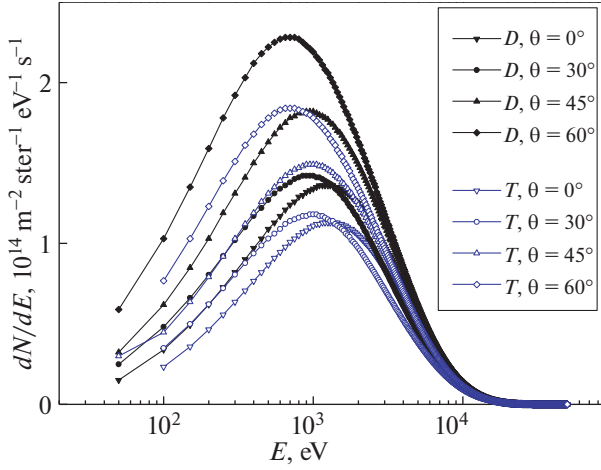
Fig. 10. Energy spectrum dN/dE of deuterium and tritium atoms bombarding the first wall of the tokamak. θ_n is the angle of incidence relative to the surface normal, $\varphi_n = 0°$. The figure is adopted from our previous work [4].

Fig. 11. Contribution of fast D and T atoms leaving plasma to sputtering of the wall fabricated from Be and W as a function of their energy for different surface potential barriers: (solid curves) a planar barrier and (dashed curves) a spherical barrier.
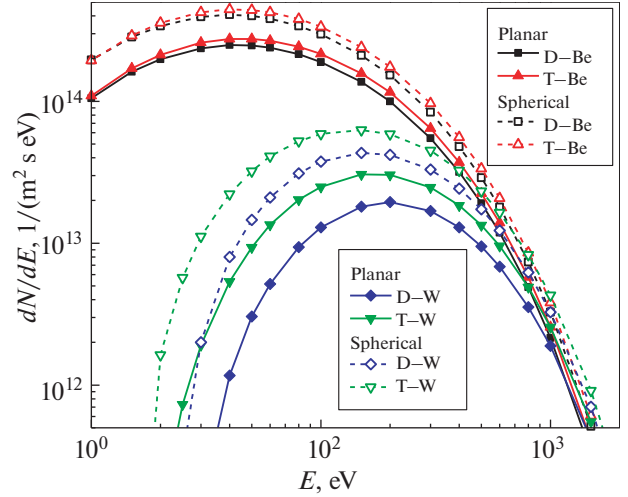
have $\Theta_\Sigma = 160°$ and $E_4 = E_0 \times 0.045$, i.e., the energy loss is four times higher. This fact explains the difference in the ratio of E_{th}/E_s for different barriers.

8. SPUTTERING OF A WALL MADE OF BERYLLIUM AND TUNGSTEN BY FAST D AND T ATOMS IN THE ITER TOKAMAK

As we mentioned before, the walls of the ITER-tokamak vessel will experience sputtering by fluxes of fast D and T atoms leaving plasma. These atoms appear due to charge exchange and photorecombination reactions of plasma ions. Fluxes of D and T atoms for typical operation regimes of the ITER tokamak [27] were calculated in [28] using the DOUBL-MC code.

Fluxes of neutral atoms were calculated for the geometry in which the point of observation was located at a distance of $r = 8.5$ m from the torus central axis and a height of $Z = 0.5$ m above the equatorial plane. Angle θ_n is the angle between the direction to the torus center and the line of sight. Angle φ_n was measured relative to the horizontal plane.

Energy spectra dN/dE of the deuterium and tritium atoms bombarding the first wall of the tokamak that were obtained using the DOUBL-MC code in [4] are presented in Figs. 10 and 11. It can be seen that the spectrum contains particles with a wide range of energies and attains maximum around 1 keV. Intensity of the flux of atoms leaving plasma increases with increase in angle θ_n, while the spectrum shifts toward lower energies.

Sputtering of the first wall as a function of energy of particles leaving plasma can be calculates as follows:

$$\frac{dQ_I}{dE} = \int_0^{2\pi}\int_0^{\frac{\pi}{2}} \frac{dN_I(E,\theta,\varphi)}{dEd\Omega} Y_I(E,\theta)\sin\theta\, d\theta\, d\varphi, \qquad (4)$$

where N_I is the number of deuterium and tritium atoms bombarding the tokamak wall, and $Y_I(E, \theta)$ is the sputtering yield of the wall material as a function of energy and angle of incidence θ for the type of bombarding atoms under consideration.

It is evident from Fig. 11 that the contribution of particles with energies in the range from 100 to 2000 eV to sputtering of beryllium is dominant, while particles with energies in the range from 500 to 4000 eV dominate in sputtering of the wall fabricated from tungsten. The observed substantial shift of the energy spectra toward higher energies in the case of W is caused by higher sputtering thresholds.

Integrating the spectra with respect to energy, we obtain the influx of the sputtered particles into plasma for various cases of the surface potential barrier (see Table 1).

Let us estimate possible concentration of impurities using the following model: sputtered particles arrive into plasma from entire surface of the tokamak wall equal to $S = 937$ m^2 and fill entire plasma volume of $V = 838$ m^3; the containment time of particles in plasma τ is assumed to be $\tau = 3$ s; the average plasma density is assumed to be equal to $n_e = 1 \times 10^{20}$ m^{-3}. The

Table 1. Fluxes of atoms sputtered by D and T atoms along with the total flux for different wall materials. Fluxes are presented in units of particles/(m^2 s). The right-hand side column represents an estimate of the relative impurity concentration in plasma in percent

		D	T	D + T	n_Z/n_e, %
Be	Planar	5.24×10^{17}	5.99×10^{17}	1.12×10^{18}	3.82
	Spherical	8.22×10^{17}	9.27×10^{17}	1.75×10^{18}	5.96
W	Planar	9.60×10^{16}	1.46×10^{17}	2.42×10^{17}	0.824
	Spherical	1.97×10^{17}	2.78×10^{17}	4.76×10^{17}	1.62

ratio of impurity concentration n_Z to average plasma density n_e is given by

$$\frac{n_Z}{n_e} = \frac{N_Z S \tau}{V n_e}, \tag{5}$$

where N_Z is the total flux of atoms sputtered by fast D and T atoms. Our estimate of Be concentration in plasma (4–6% of the electron density) is somewhat higher than the estimate reported in [4] (2.5–4.2%). Estimated fluxes for the wall fabricated from Be are a factor of 3–6 higher that the corresponding results obtained in [29] where the flux of $Q_{Be} = 3 \times 10^{17}$ atoms/(s m^2) was reported for our experimental geometry. Apparently, the difference is caused by the fact that underestimated values of sputtering yields obtained by means of the SRIM [6] code were used in [29]. We believe that Be concentration at this level is not harmful for tokamak operation since it is much lower than the lethal concentration of ≈25% [30].

In the case of W, we estimate the concentration of tungsten in plasma to be at the level of 0.8–1.6% of the electron density, which is substantially higher than the lethal concentration of 0.2% [31]. Hence, the calculated flux of the sputtered W atoms upon bombardment of the tungsten wall by D and T atoms leaving plasma makes the prospect of using a tungsten wall doubtful.

Let us estimate propagation of sputtered Be and W atoms through the layer of the near-wall plasma. The spatial distributions of electron temperature $T_e(x)$ and electron density $n_e(x)$ were adopted from [29]. Distance L to the separatrix was assumed to be equal to 10 cm. According to our calculations, the average energy of the sputtered Be atoms was equal to $E_{av} \approx 12.5$ eV, white that of the W atoms was equal to $E_{av} \approx 20$ eV. Beam attenuation upon propagation of distance L was calculated using the following expression:

$$\eta = \exp\left[-\frac{\int_0^L n_e(x) R[T_e(x)]dx}{v_{at}}\right], \tag{6}$$

where $R[T_e(x)] = \langle \sigma_i \cdot v_e \rangle$ is the rate coefficient of ionization, σ_i is the ionization cross section, and v_e is the electron velocity. Product $\sigma_i \cdot v_e$ was averaged taking into account the Maxwellian velocity distribution of electrons for specific electron temperature. Parameter v_{at} represents the average velocity of the sputtered atoms. The values of $R(T_e)$ for Be were adopted from [32]. We calculated the values of $R(T_e)$ for tungsten using the ionization cross section taken from [33].

According to our estimates, the sputtered atoms will be totally ionized near the wall under typical parameters of the ITER plasma. The flux of Be atoms will be attenuated by a factor of $1/e$ after propagation of 5 cm from the wall. The corresponding attenuation factor on the path to the separatrix will be $\eta = 6.7 \times 10^{-3}$. The $1/e$ attenuation of the beam of W atoms will take place upon propagation of a distance equal to 12 cm from the wall, while attenuation factor on the path to the separatrix will be equal to $\eta = 1.5 \times 10^{-34}$. Atoms will be unable to reach the separatrix and will become ionized. The complex transport codes [34–38] have to be used in order to calculate the influx of impurity atoms into the hot plasma region more accurately.

Our estimates establish the boundary conditions for the fluxes of sputtered particles and their energies at the plasma boundary. We took into consideration only wall sputtering by the fluxes of neutral atoms leaving plasma. The action from the plasma ions and irradiation by neutrons can only increase these fluxes. Other parameters, such as fragility, defect formation, saturation by tritium, utilization, etc. should be taken into account when choosing the wall material.

CONCLUSIONS

In this work, we presented the results of simulation of the sputtering yields of beryllium and tungsten by H, D, T, He, Be, C, N, O, Ne, Ar, and W atoms in the range of collision energies from 10 to 100000 eV that are required for estimating the degree of sputtering of the first wall fabricated from beryllium and the divertor plates fabricated from tungsten in the ITER tokamak.

We demonstrated that surface relief has a major impact on the obtained results. Calculation for the

case of a planar surface and a surface consisting of points showed that these two limiting cases define the range in which the sputtering yield can vary. In other words, the experimental data are expected to fall into this "corridor" depending on the quality of preparation of the target surface.

The obtained information on the average energies of the sputtered atoms and their angular distributions is important for estimating the influx of the sputtered particles into the tokamak plasma.

Using the obtained sputtering yields, we also calculated the fluxes of atoms sputtered upon bombardment of the wall fabricated from Be and W by fast D and T atoms leaving plasma.

FUNDING

CONFLICT OF INTEREST

The authors of this work declare that they have no conflicts of interest.

OPEN ACCESS

REFERENCES

1. P. Yu. Babenko, V. S. Mikhailov, and A. N. Zinoviev, Tech. Phys. Lett. **49** (4), 80 (2023). https://doi.org/10.21883/TPL.2023.04.55887.19432

2. P. Yu. Babenko, V. S. Mikhailov, A. P. Shergin, and A. N. Zinoviev, Tech. Phys. **93** (5), 662 (2023). https://doi.org/10.21883/TP.2023.05.56074.12-23

3. V. S. Mikhailov, Yu. Babenko, A. P. Shergin, and A. N. Zinov'ev, J. Exp. Theor. Phys. **137**, 413 (2023). https://doi.org/10.1134/S106377612309011X

4. P. Yu. Babenko, M. I. Mironov, V. S. Mikhailov, and A. N. Zinoviev, Plasma Phys. Controlled Fusion **62**, 045020 (2020). https://doi.org/10.1088/1361-6587/ab7943

5. V. I. Afanasyev, M. I. Mironov, V. G. Nesenevich, M. P. Petrov, and S. Ya. Petrov, Plasma Phys. Controlled Fusion **55**, 045008 (2013). https://doi.org/10.1088/0741-3335/55/4/045008

6. J. F. Ziegler and J. P. Biersack, SRIM Software. http://www.srim.org. Cited June 25, 2023.

7. *Sputtering by Particle Bombardment*, Ed. by R. Behrisch and W. Eckstein (Springer, Berlin, 2007). https://doi.org/10.1007/978-3-540-44502-9

8. *Atomic and Plasma-Material Interaction Data for Fusion*, Ed. by R. E. H. Clark (IAEA, Vienna, 1998), Vol. 7/B.

9. F. Granberg, J. Byggmästar, and K. Nordlund, J. Nucl. Mater. **556**, 153158 (2021). https://doi.org/10.1016/j.jnucmat.2021.153158

10. C. Björkas and K. Nordlund, J. Nucl. Mater. **439**, 174 (2013). https://doi.org/10.1016/j.jnucmat.2013.04.036

11. A. Lyashenko, E. Safi, J. Polvi, F. Djurabekova, and K. Nordlund, J. Nucl. Mater. **542**, 152465 (2020). https://doi.org/10.1016/j.jnucmat.2020.152465

12. C. Björkas, N. Juslin, H. Timko, K. Vörtler, K. Nordlund, K. Henriksson, and P. Erhart, J. Phys.: Condens. Matter **21**, 445002 (2009). https://doi.org/10.1088/0953-8984/21/44/445002

13. M. V. Prokof'ev, V. V. Svetukhin, and M. Yu. Tikhonchev, Izv. Samar. Nauchn. Tsentra Ross. Akad. Nauk **15**, 1024 (2013).

14. A. N. Zinov'ev and P. Yu. Babenko, JETP Lett. **115**, 560 (2022). https://doi.org/10.1134/S0021364022100526

15. A. N. Zinoviev and K. Nordlund, Nucl. Instrum. Methods Phys. Res., Sect. B **406**, 511 (2017). https://doi.org/10.1016/J.NIMB.2017.03.047

16. A. N. Zinoviev, P. Yu. Babenko, and K. Nordlund, Nucl. Instrum. Methods Phys. Res. Sect. B **508**, 10 (2021). https://doi.org/10.1016/j.nimb.2021.10.001

17. D. Primetzhofer, S. Rund, D. Roth, D. Goebl, and P. Bauer, Phys. Rev. Lett. **107**, 163201 (2011). https://doi.org/10.1103/PhysRevLett.107.163201

18. A. Mann and W. Brandt, Phys. Rev. B: Condens. Matter Mater. Phys. **24**, 4999 (1981). https://doi.org/10.1103/PhysRevB.24.4999

19. W. Eckstein, *Computer Simulations of Ion-Solid Interactions* (Springer, Berlin, 1991).

20. G. Falcone and F. Gullo, Phys. Lett. A **125**, 432 (1987). https://doi.org/10.1016/0375-9601(87)90178-2

21. P. Sigmund, Phys. Rev. **184**, 383 (1969). https://doi.org/10.1103/PhysRev.184.383

22. R. Behrisch, G. Maderlechner, B. M. U. Scherzer, and M. T. Robinson, Appl. Phys. **18**, 391 (1979). https://doi.org/10.1007/BF00899693

23. D. S. Meluzova, P. Yu. Babenko, A. N. Zinoviev, and A. P. Shergin, Tech. Phys. Lett. **46**, 1227 (2020). https://doi.org/10.1134/S1063785020120226

24. X. Yang and A. Hassanein, Appl. Surf. Sci. **293**, 187 (2014). https://doi.org/10.1016/j.apsusc.2013.12.129

25. Y. Yamamura and H. Tawara, At. Data Nucl. Data Tables **62**, 149 (1996).
https://doi.org/10.1006/ADND.1996.0005

26. S. Brezinsek and JET-EFDA contributors, J. Nucl. Mater. **463**, 11 (2015).
https://doi.org/10.1016/j.jnucmat.2014.12.007

27. V. I. Afanasyev, F. V. Chernyshev, A. I. Kislyakov, S. S. Kozlovsky, B. V. Lyublin, M. I. Mironov, A. D. Melnik, V. G. Nesenevich, M. P. Petrov, and S. Ya. Petrov, Nucl. Instrum. Methods Phys. Res., Sect. A **621**, 456 (2010).
https://doi.org/10.1016/j.nima.2010.06.201

28. M. I. Mironov, F. V. Chernyshev, V. I. Afanasyev, A. D. Melnik, A. S. Navolotsky, V. G. Nesenevich, M. P. Petrov, and S. Ya. Petrov, Plasma Phys. Rep. **47**, 18 (2021).
https://doi.org/10.1134/S1063780X21010104

29. S. Makarov and E. Kaveeva, MATEC Web Conf. **245**, 13002 (2018).
https://doi.org/10.1051/matecconf/201824513002

30. V. I. Gervids and V. I. Kogan, JETP Lett. **21**, 150 (1975).

31. D. M. Meade, Nucl. Fusion **14**, 289 (1974).
https://doi.org/10.1088/0029-5515/14/2/017

32. K. L. Bell, H. B. Gilbody, J. G. Hughes, A. E. Kingston, and F. J. Smith, J. Phys. Chem. Ref. Data **12**, 891 (1983).
https://doi.org/10.1063/1.555700

33. D.-H. Kwon, Y.-J. Rhee, and Y.-K. Kim, Int. J. Mass Spectrom. **252**, 213 (2006).
https://doi.org/10.1016/j.ijms.2006.03.007

34. A. S. Kukushkin, H. D. Pacher, V. Kotov, G. W. Pacher, and D. Reiter, Fusion Eng. Des. **86**, 2865 (2011).
https://doi.org/10.1016/j.fusengdes.2011.06.009

35. I. Yu. Senichenkov, E. G. Kaveeva, E. A. Sytova, V. A. Rozhansky, S. P. Voskoboynikov, I. Yu. Veselova, D. P. Coster, X. Bonnin, F. Reimold, and the ASDEX-Upgrade Team, Plasma Phys. Controlled Fusion **61**, 045013 (2019).
https://doi.org/10.1088/1361-6587/ab04d0

36. K. Jesko, Y. Marandet, H. Bufferand, J. P. Gunn, H. J. van der Meiden, and G. Ciraolo, Contrib. Plasma Phys. **58**, 798 (2018).
https://doi.org/10.1002/ctpp.201700186

37. V. Rozhansky, E. Kaveeva, I. Senichenkov, and E. Vekshina, Plasma Phys. Controlled Fusion **60**, 035001 (2018).
https://doi.org/10.1088/1361-6587/aaa11a

38. F. Köchl, A. Loarte, E. de la Luna, V. Parail, G. Corrigan, D. Harting, I. Nunes, C. Reux, F. G. Rimini, A. Polevoi, M. Romanelli, and JET Contributors, Plasma Phys. Controlled Fusion **60**, 074008 (2018).
https://doi.org/10.1088/1361-6587/aabf52